
Article:
Molinar-Díaz, J., Woodliffe, J.L., Milborne, B. et al. (7 more authors) (2023) Ferromagnetic cytocompatible glass-ceramic porous microspheres for magnetic hyperthermia applications. Advanced Materials Interfaces. 2202089. ISSN 2196-7350

https://doi.org/10.1002/admi.202202089

ADVANCED MATERIALS INTERFACES
Open Access
www.advmatinterfaces.de

Ferromagnetic Cytocompatible Glass-Ceramic Porous Microspheres for Magnetic Hyperthermia Applications

*Jesús Molinar-Díaz, John Luke Woodliffe, Benjamin Milborne, Lauren Murrell, Md Towhidul Islam, Elisabeth Steer, Nicola Weston, Nicola A. Morley, Paul D. Brown, and Ifty Ahmed**

Highly porous, ferromagnetic glass-ceramic P40-Fe_3O_4 microspheres (125–212 µm) with enhanced cytocompatibility have been manufactured for the first time via a facile, rapid, single-stage flame spheroidization process. Dispersions of Fe_3O_4 and $Ca_2Fe_2O_5$ domains (≈10 µm) embedded within P40 ($40P_2O_5$-16CaO-24MgO-$20Na_2O$ in mol%) phosphate-based glass matrices show evidence for remanent magnetization (0.2 $Am^2\ kg^{-1}$) and provide for controlled induction heating to a constant level of 41.9 °C, making these materials highly appropriate for localized magnetic hyperthermia applications. Complementary, cytocompatibility investigations confirm the suitability of P40-Fe_3O_4 porous microspheres for biomedical applications. It is suggested that the flame-spheroidization process opens up new opportunities for the development of innovative synergistic biomaterials, toward bone-tissue regenerative applications.

1. Introduction

Cancer treatment and therapy is one of the most challenging problems for modern medicine.[1] The main cancer treatments of radiotherapy, chemotherapy, and surgery, often used in combination, have demonstrated effectiveness in the eradication of primary tumors in the clinical setting.[2] However, the benefits of these strategies are usually accompanied by harmful side effects: e.g., (*i*) conventional chemotherapy is not tumor-selective, equally damaging both healthy and cancerous cells;[3,4] (*ii*) radiotherapy delivered to tumors is dose-limited due to toxicity effects on surrounding tissue, resulting in decreased effectiveness;[5,6] and (*iii*) cancer can reappear post-surgical removal of tumors, arising from residual malignant cells and cancer stem cells.[2] Also, significant amounts of healthy tissue may be lost as a consequence of tumor removal via surgery. The success of a cancer treatment may be measured by its ability to eliminate malignant cells whilst minimizing damage to healthy tissue and maintaining functionality. Also, the regeneration of healthy tissue depends on the survival of stem cells post-treatment. Accordingly, complementary clinical strategies are required to eradicate the resistance of malignant cells whilst maintaining patient well-being and quality of life.

Hyperthermia (HT), a method of inducing cancer cell death by the application of heat, uses non-ionizing radiation or convective methods to increase temperature (to ≈40–45 °C) in targeted regions of the body, whilst magnetic hyperthermia (MHT) uses heat generated by localized ferromagnetic particles exposed to an alternating magnetic field.[7–9] MHT has been explored in combination with radiotherapy and chemotherapy as a strategy for drug-delivery.[10] The main benefit of MHT relates to its ability to treat site-specific cancer whilst avoiding hazardous systemic effects.[11] Furthermore, MHT is minimally invasive (i.e., delivered intratumorally or intravenously by injection), with mild side effects compared to radiotherapy or chemotherapy,[10] and shows synergistic effects with many cancer treatments, e.g., brachytherapy,[12] drug-delivery,[13] immunotherapy,[14] and gene therapy.[15]

J. Molinar-Díaz, J. L. Woodliffe, B. Milborne, L. Murrell, M. T. Islam, P. D. Brown, I. Ahmed
Advanced Materials Research Group
Faculty of Engineering
University of Nottingham
University Park, Nottingham NG7 2RD, UK
E-mail: ifty.ahmed@nottingham.ac.uk

The ORCID identification number(s) for the author(s) of this article can be found under https://doi.org/10.1002/admi.202202089.

DOI: 10.1002/admi.202202089

E. Steer, N. Weston, P. D. Brown
Nanoscale and Microscale Research Centre
University of Nottingham
University Park, Nottingham NG7 2RD, UK

N. A. Morley
Department of Materials Science and Engineering
University of Sheffield
Sheffield S1 3JD, UK

M.T.I. School of Physical Sciences
University of Kent
Canterbury CT2 7NZ, UK, and Department of Applied Chemistry and Chemical Engineering
Faculty of Engineering
Noakhali Science and Technology University
Noakhali 3814, Bangladesh

Iron oxide nanoparticles (Fe_3O_4 magnetite and γ-Fe_2O_3 maghemite) have been most investigated for MHT, due to their promising combination of non-toxicity and magnetic properties.[16] Indeed, the use of superparamagnetic iron oxide nanoparticles to deliver heat to various tumor types has been reported, including prostate[17] and glioblastoma.[18] Further, aminosilane-coated ferrofluid, combined with a alternating magnetic field system, has been used clinically to target glioblastoma tumors.[10] Magnetic bone cements,[19] glass-ceramic thermoseeds[20] and Fe-based nanoparticles[21] have also been developed for bone cancer therapy via MHT. Nevertheless, despite multiple ongoing trials, MHT has still not achieved regular use in clinical practice, mainly due to its inability to effectively heat cancerous cells.[22] It is recognized that the action of a single nanoparticle is insufficient for local hyperthermia,[23] with agglomeration of a large number of superparamagnetic nanoparticles needed to generate sufficient heat to damage tumor cells.[24,25] However, agglomeration can affect the superparamagnetic expression of such nanoparticles, compromising heat performance.[24,26]

It is suggested a dispersion of micrometer-scale, ferro- or ferrimagnetic material, in a suitable matrix, could be used instead of a large number of superparamagnetic nanoparticles.[27] Further, a micro-system combining bone-tissue regeneration, cancer thermotherapy and biomechanical support, such as the conjugation of an iron oxide ferromagnetic phase (e.g., magnetite) with a bioactive glass matrix, could provide a promising approach for cancer treatments mediated via MHT, e.g., targeting bone oncology.[28]

Bioactive glasses are not only of interest to promote the regeneration of soft and hard tissue, but can also be made to exhibit angiogenic properties (i.e., to stimulate growth of new blood vessels).[29] Accordingly, glass-ceramics are considered to offer great potential in the healthcare sector for tissue engineering and regenerative applications. Bioactive glass compositions have been developed to bond with soft (e.g., skin, nerve, ligament) and hard tissue (bone).[30–32] Further, osteoconductivity, osteoinductivity, angiogenic potential and antibacterial properties are characteristic of many bioactive glass phases.[33]

Moreover, developing magnetic glass ceramics into porous morphologies could expedite complementary clinical strategies for tumor treatment and facilitate repeated MHT treatment to help safeguard against tumor regrowth. Porous microspheres possess large surface areas and can be manufactured with large external and internal (usually interconnected) pores, to enable delivery of drugs, cells or other biologics.[34–36] There are various strategies for the production of porous bioactive glasses and/or ceramics, including the incorporation of a removable space holder (via sintering),[37] sol–gel,[38] gel–cast forming,[39] polymer foam replication,[40] solid-free form (3D printing),[41] and more recently flame spheroidization.[42] The single-stage, flame-process is a rapid, cost-effective and highly promising technique for large-scale production of porous glass and glass-ceramic microspheres.[43] Flame spheroidization may also be used for the manufacture of magnetic, porous and dense, ceramic microspheres.[44]

The overarching need is to balance magnetic properties and matrix cytocompatibility for the safe application and performance of MHT. In this context, we report on the development of novel, ferromagnetic, cytocompatible, glass-ceramic microspheres, with high levels of interconnected porosity, manufactured via our single-stage flame spheroidization process, as an attractive candidate for MHT applications.

2. Experimental Section

2.1. Starting Materials

The starting materials were as-supplied feedstock powders of iron (II, III) oxide (Fe_3O_4; ≤45 μm, 98.1%; Inoxia, UK); calcium carbonate ($CaCO_3$, 98%; Fisher Scientific UK Ltd); and chemical precursors used for glass production, i.e., calcium hydrogen phosphate ($CaHPO_4$), magnesium hydrogen phosphate trihydrate ($MgHPO_4{\cdot}3H_2O$), sodium dihydrogen phosphate (NaH_2PO_4) and phosphorous pentoxide (P_2O_5) (Merck).

2.2. Glass Formulation

The quaternary phosphate-based glass 40-P_2O_5-16CaO-24MgO-20Na_2O (in mol%), denoted P40, was produced using the melt-quench technique. 21.8 g of $CaHPO_4$, 41.8 g of $MgHPO_4.3H_2O$, 24 g of NaH_2PO_4, and 56.8 g of P_2O_5 were placed into a platinum-rhodium alloy crucible (Birmingham Metal Company, UK), mixed using a stainless-steel spatula, and dried at 350 °C for 30 min in a furnace. The mixture was then melted at 1150 °C for 90 min, poured onto a steel plate and left to cool to room temperature.[45] The glass was then ground to a fine microparticle powder using a milling machine (Retsch PM100 Planetary Ball Mill) for 5 min and sieved (stainless steel frame; 203 × 50 mm^2; ≥63 μm and ≥125 μm mesh; VWR International) to collect particles in the size range of 63–125 μm.

2.3. Microsphere Preparation via Flame Spheroidization

3 g of Fe_3O_4 (≤ 45 μm) and 3 g of P40 (63–125 μm) (1:1 mass ratio) were combined using a vortex mixer. The P40-Fe_3O_4 powders were then mixed with 18 g of $CaCO_3$ (as porogen, ≤ 63 μm) (1:3 mass ratio). The prepared powders were then processed into porous microspheres using a thermal spray gun (MK74, Metallisation Ltd, UK) coupled with oxygen-acetylene (O_2/C_2H_2: 1:1 gas flow ratio).[44] The flame spheroidized products were washed using acetic acid (5 M) for 2 min and deionized water for 1 min, and then dried at 37 °C for 24 h. The resultant microspheres were then sieved to a size range 125–212 μm (stainless steel frame; 203 × 50 mm^2; ≥ 125 μm and ≥212 μm mesh; VWR International) and stored in glass vials for characterization. The Fe_3O_4 and P40 powders alone were also flame-processed individually (without porogen, unsieved), to serve as controls.

Sieved P40-Fe_3O_4 microspheres products were embedded in cold epoxy resin and sectioned by sequential mechanical grinding (400, 800, and 1200 SiC papers) and polishing (6 and

1 µm diamond paste). The polished samples were then cleaned using deionized water and industrial methylated spirit (IMS), and dried before carbon coating.

2.4. Materials Characterization

2.4.1. Scanning Electron Microscopy

Topographic imaging of the sieved, flame-processed products was performed via scanning electron microscopy (SEM; FEI XL30; 10 kV; spot size 5; 25.3 mm working distance; secondary electron (SE) imaging mode). Measurement of microsphere size distributions and surface pores diameters were performed using ImageJ 1.51 h software (National Institutes of Health, USA).

2.4.2. X-Ray Diffractometry

Structural characterization of the microsphere products was performed by X-ray diffractometry (XRD; Bruker D8 Advance, Da Vinci design with LYNXEYE XE-T detector in 1D mode; Cu Kα radiation (λ = 0.15406 nm); 40 kV and 40 mA; step size 0.02°; total time/step 29.8 s per datapoint; 21 °C).

2.4.3. Mineral Liberation Analysis

Chemical investigation of the sectioned microspheres was performed via backscattered electron (BSE) imaging and SEM-based mineral liberation analysis (MLA; FEI Quanta600 MLA, 20 kV; spot size 7), equipped with energy-dispersive X-ray spectroscopy (EDS; Bruker software, 12.9 mm working distance) and data acquisition software for automated mineralogy (Bruker/JKTech/FEI). For EDS quantification, Bruker software assumed oxides were utilized, with compositional measurements averaged across 15 different point locations.

2.4.4. SQUID Magnetometry

Complementary magnetic characterization was performed using superconducting quantum interference device magnetometry (SQUID; Quantum Design MPMS-3 system; VSM mode; vibration amplitude 1.5 mm; 26.9 °C). The powders were encapsulated within gelatin capsules before being mounted on the sample holder.

2.4.5. High Frequency Induction

The heating of microsphere products was performed via high frequency induction (Cheltenham Induction Heating Ltd; 100–250 V; 120–350 W; 1.2–1.4 A; 204 kHz). Glass vials containing the microspheres were placed at the center of a water-cooled copper coil generating an alternating magnetic field, whilst temperature was measured using a fiber optic sensor (Neoptix Reflex Signal Conditioner). Control samples of processed Fe_3O_4 and P40 microspheres were also investigated. All measurements were recorded in triplicate (n = 3).

2.5. Cytocompatibility

2.5.1. Cell Culturing

The microsphere products were sterilized by washing in ethanol (100%) followed by complete evaporation overnight in a sterile environment at room temperature. The human osteoblast-derived cell line MG-63 (European collection of authenticated cell cultures—ECACC) was seeded onto the microspheres at a density of 10 000 cells cm^{-2} in 300 µL of standard cell culture medium; comprising Dulbecco's Modified Eagle Medium (DMEM) supplemented with 10% fetal calf serum, 1% penicillin and streptomycin, 1% L-Glutamine, 1% of non-essential amino acids and 1.5% ascorbic acid. Cells were seeded on 10 mg of sterile microspheres in low-adherent 48-well plates previously coated with 1% (w/v) solution of poly(2-hydroxyethyl methacrylate) (poly-HEMA, Merck) and Ethanol 95% in standard cell culture medium. Cells were incubated at 37 °C and 5% CO_2, with media refreshed every 48 h. Two independent experiments were performed, with 3 experimental replicates for each condition.

2.5.2. Cell Metabolic Activity

MG-63 cell metabolic activity was evaluated using an Alamar Blue assay at days 2 and 7. Following removal of standard cell culture medium and washing with phosphate-buffered saline, 300 µL of Alamar Blue solution (1:9 Alamar blue:Hanks Balanced Salt Solution) was added to each well plate and incubated for 90 min at 37 °C and 5% CO_2, followed by a further 10 min on a shaker at 150 rpm. Three aliquots of 100 µL were transferred to a 96-well plate. An FLx800 fluorescence microplate reader (BioTek Instruments Inc.) was used to measure fluorescence at 530-nm excitation and 590-nm emission wavelengths.

2.5.3. Statistical Analysis for Cell Culture Investigations

Two independent cell culture experiments were performed with results shown as "*mean ± standard error of mean*" (unless otherwise stated). Statistical analysis was performed using Prism software (version 9.2.0, GraphPad Software, San Diego, CA). Two-way analysis of variance was calculated followed by a Tukey's multiple comparison test. Mean difference was considered to be significant at p = 0.05 corresponding to a 95% confidence level.

2.5.4. Environmental Scanning Electron Microscopy

At day 7, cells were fixed using 4% paraformaldehyde. Fixed cells decorating the microspheres were imaged using an environmental scanning electron microscope (ESEM; FEI Quanta

650 ESEM; 10 kV; spot size 5; 6.7 mm working distance; 4.76 torr; 2.0 °C; humidity 89.5%).

3. Results

3.1. Microsphere Morphologies

Figure 1a presents a representative, low-magnification SE image of the flame spheroidized P40-Fe_3O_4 microsphere products (125–212 μm). To the best of our knowledge, this is the first demonstration of magnetic-cytocompatible glass ceramic microspheres showing exceptionally high levels of porosity. Figure 1b shows a P40-Fe_3O_4 porous microsphere in detail, while Figure 1c highlights the interconnected nature of the porosity. For comparison, Figure 1d,e present SE images of flame processed Fe_3O_4 and P40 dense microspheres, respectively, as used for magnetometry, induction heating and cytocompatibility control investigations. Both samples were manufactured under the same processing conditions as for P40-Fe_3O_4.

The P40-Fe_3O_4 products showed the largest number of highly porous microspheres within the 141–180 μm size range (Figure S1a, Supporting Information), while dense Fe_3O_4 and P40 controls exhibited smaller microspheres in the range ≈20–100 μm and ≈30–150 μm, respectively. It was noted that smaller P40-Fe_3O_4 products in the 63–125 μm size range tended to be formed irregular shaped particles exhibiting lower levels of porosity (see Figure S2, Supporting Information). For the case of well-defined P40-Fe_3O_4 porous microspheres (125 – 212 μm), the surface pore diameters exhibited values in the range 0.9 to 56.2 μm (Figure S1b, Supporting Information; mean 2.8 μm; median 1.9 μm; SD 3.79; n = 490 pores measured from three different microspheres).

3.2. Structural Characterization

Figure 2 presents XRD patterns for the flame spheroidized P40-Fe_3O_4 porous microspheres, as compared to the dense Fe_3O_4 and P40 microspheres (as control). The diffractogram for P40 processed in isolation exhibited a characteristic glass curve consistent with its amorphous nature; while that for processed Fe_3O_4 confirmed retention of crystalline Fe_3O_4 (ICDD PDF no. 01-087-0246) along with the presence of a small amount of Fe_2O_3 (ICDD PDF no. 00-033-0664). Interestingly, the diffractogram for processed P40-Fe_3O_4 revealed the presence of crystalline $Ca_2Fe_2O_5$ (ICDD PDF no. 00-047-1744), along with (unreacted) Fe_3O_4 and $CaCO_3$ (ICDD PDF no. 01-071-3699), with slight curvature of the baseline consistent with the presence of amorphous P40.

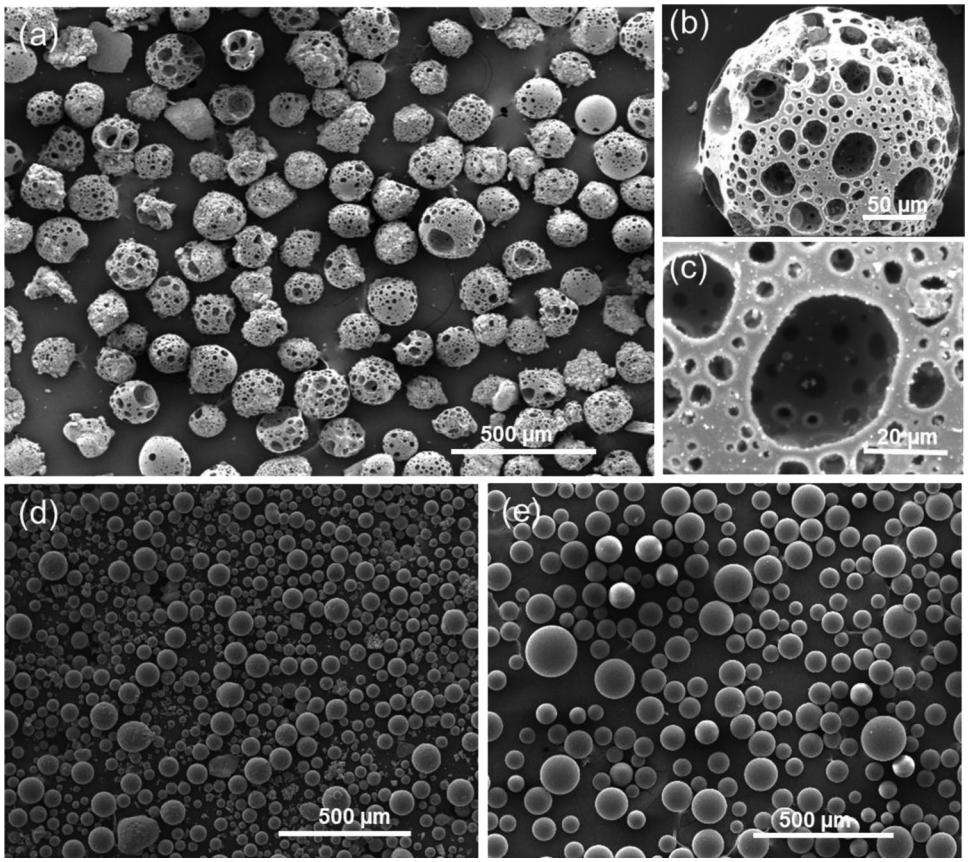

Figure 1. SE images of flame spheroidized a) P40-Fe_3O_4 porous microspheres (125–212 μm); with b) details of a porous microsphere; and c) highlight of microsphere interconnected porosity. Flame spheroidized, unsieved d) Fe_3O_4 dense microspheres (≈20–100 μm), and e) P40 dense microspheres (≈30–150 μm), used as controls.

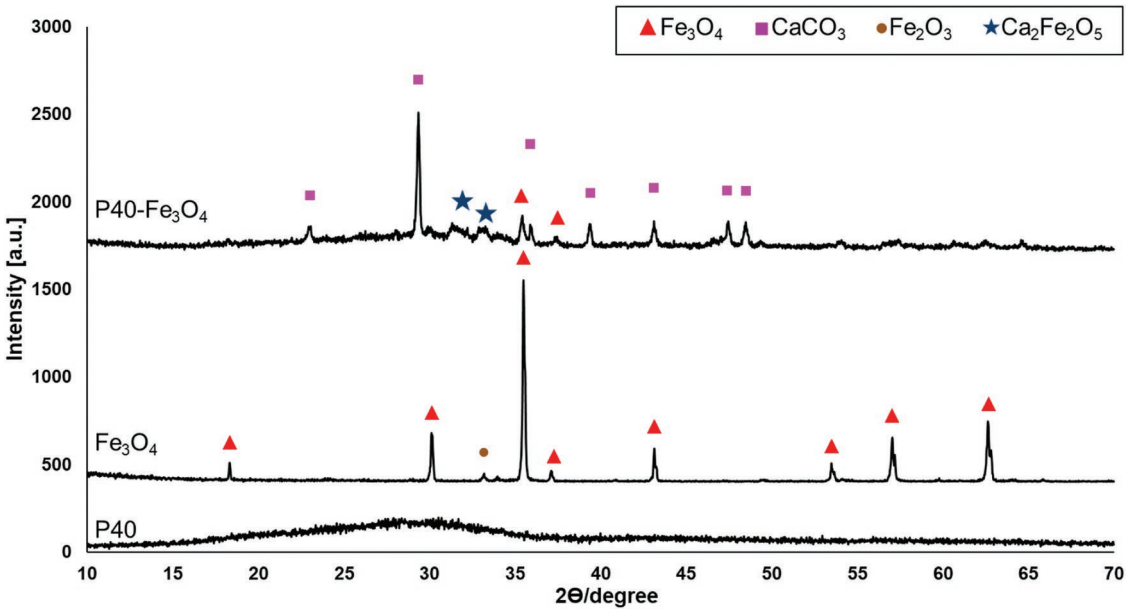

Figure 2. X-ray diffractograms for flame spheroidized, highly porous, P40-Fe_3O_4 microspheres, as compared to Fe_3O_4 and P40 dense microsphere control samples. Miller indices tabulated in Table S1 (Supporting Information).

3.3. Chemical Analysis

Figure 3a represents a BSE image of resin embedded and sectioned P40-Fe_3O_4 microspheres, evidencing very high levels of interconnected porosity. Mineral mapping (Figure 3b) revealed a variety of products dominated by Ca-P40-Fe, P40-Fe and $Ca_2Fe_2O_5$, along with unreacted P40, $CaCO_3$ and Fe_3O_4 (Figure 3c). A total of 24637 particles were quantified via MLA software using a standard 70% matching threshold (see Figure S3, Supporting Information; including key for the compositional assignments).

Further, **Figure 4** presents a detailed EDS elemental map of sectioned P40-Fe_3O_4 porous microspheres, highlighting a distribution of FeO-rich domains (≈10 µm sized) embedded within the microspheres (125–212 µm). A summary of the compositions of FeO-rich and FeO-poor regions of the microspheres is presented in **Table 1**. Notably, elevated levels of CaO were associated with FeO-rich regions.

3.4. Magnetic Properties of Microspheres

Figure 5 presents magnetization curves for flame-processed P40-Fe_3O_4 porous microspheres, Fe_3O_4 dense microspheres, and P40 dense microspheres, respectively. Importantly, the P40-Fe_3O_4 porous microspheres and Fe_3O_4 dense microspheres both revealed typical hysteresis loops indicative of ferromagnetic behavior. As summarized in **Table 2**, the Fe_3O_4 microspheres showed the highest levels of magnetic saturation, while the P40 dense microspheres showed no magnetic saturation,

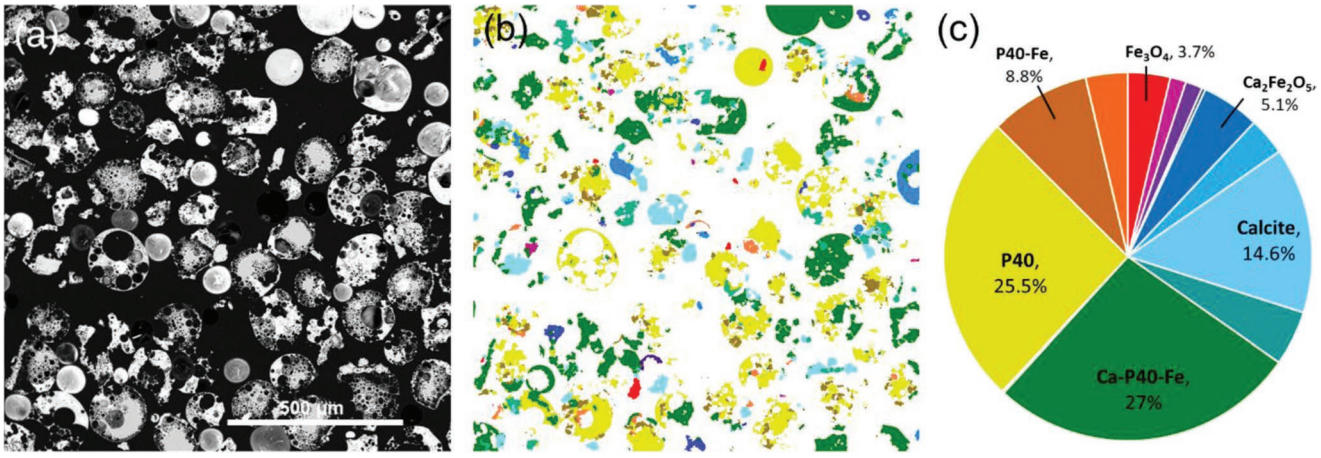

Figure 3. Sectioned, flame-processed, P4O-Fe_3O_4 microspheres: a) BSE image highlighting microsphere porosity; b) MLA compositional map and c) summary chart of mineral proportions (wt%) demonstrating a mixed phase product comprising primarily iron oxide decorated P40. (Color code, mineral references, modal minerology, and full mineral mapping included in Figure S3, Supporting Information.)

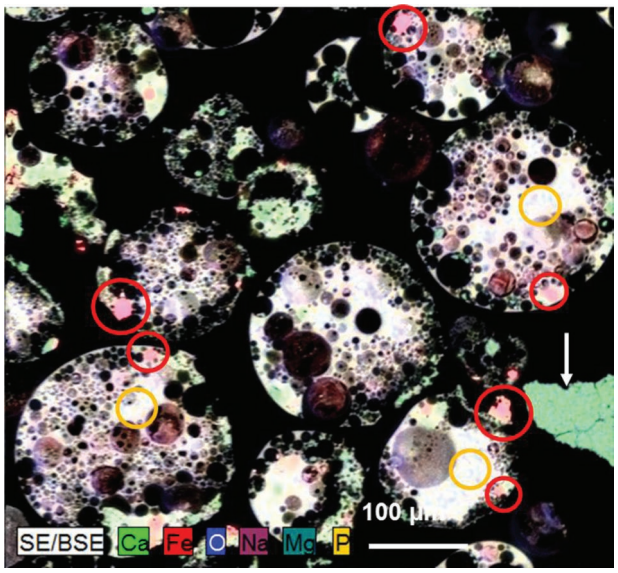

Figure 4. EDS elemental mapping of sectioned, flame-processed, P40-Fe_3O_4 microspheres. Red circles denote FeO-rich regions. Yellow circles denote FeO-poor regions. White arrow highlights an unreacted $CaCO_3$ particle. (Complementary BSE image and individual EDS elemental maps are included in Figure S4, Supporting Information.)

as anticipated. Notably, highly porous P40-Fe_3O_4 microspheres exhibited magnetic saturation at 4 $Am^2\ kg^{-1}$ and a lower but significant value of remanent magnetization, at 0.2 $Am^2\ kg^{-1}$, as compared to dense Fe_3O_4 microspheres.

3.5. Induction Heating

Figure 6 illustrates the evolution of temperature of induction heated highly porous P40-Fe_3O_4 microspheres, as compared to reference dense Fe_3O_4 and P40 microspheres. Experimental parameters for the induction heating experiments are summarized in **Table 3**. The Fe_3O_4 microspheres exhibited the highest levels of induction heating, reaching up to ≈140 °C, but with complete lack of heating control. Conversely, the P40 microspheres showed no induction heating at all, as anticipated. Notably, the P40-Fe_3O_4 porous microspheres exhibited highly controlled heating profiles, to a constant level of 41.9 °C, which remained stable upon voltage decrease (from 250 down to 100 V after 40 s; Table 3); making them highly appropriate for MHT applications. It is noted that the application of lower voltages of 50 and 150 V, respectively, to the P40-Fe_3O_4 microspheres resulted in slower heating rates (see Figure S5, Supporting Information). For the case of the Fe_3O_4 samples, a voltage decrease was applied at 10 s and stopped at ≈80 s due to the uncontrolled temperature rise (Figure 6).

Table 1. Molar constituents of highlighted regions of flame-processed P40-Fe_3O_4 microspheres (Figure 4).

	Na_2O [wt%] ± SD	MgO [wt%] ± SD	CaO [wt%] ± SD	P_2O_5 [wt%] ± SD	FeO [wt%] ± SD
FeO-rich	9.3 ± 4.8	8.4 ± 3.2	32.2 ± 9.2	44.8 ± 7.4	5.4 ± 5.8
FeO-poor	14.7 ± 0.2	11.6 ± 0.2	11.7 ± 0.2	61.9 ± 0.3	0.1 ± 0.1

3.6. Cytocompatibility

For cytocompatibility assessment, the MG-63 cell line in direct contact response to P40-Fe_3O_4 porous microspheres was evaluated at day 2 and day 7, via measurement of cell metabolic activity (**Figure 7**a) and compared with the response to dense Fe_3O_4 and P40 microspheres. Analysis at day 2 revealed the metabolic response to be significantly higher for cells exposed to P40-Fe_3O_4 microspheres, compared to the controls ($p << 0.0007$). Notably, no significant difference was returned for cells exposed to P40-Fe_3O_4 microspheres and TCP (control) on day 2.

On day 7, P40-Fe_3O_4 porous microspheres presented no significant difference in cell response compared to day 2. Conversely, Fe_3O_4 dense microspheres showed lower cellular response, whilst P40 dense microspheres presented higher levels of metabolic activity. Evidently, P40-Fe_3O_4 porous microspheres showed higher levels of metabolic activity on day 7, as compared to Fe_3O_4 and P40 controls in isolation. Additionally, P40-Fe_3O_4 porous microspheres and TCP presented significant difference as a consequence of a TCP cell response increment.

Figure 7b,c presents high-magnification ESEM images of MG-63 cell/P40-Fe_3O_4 porous microsphere interactions, at day 7, demonstrating that the cells adhere strongly to the surface whilst being guided by surface texture.

4. Discussion

This first report on the manufacture and characterization of cytocompatible, highly porous P40-Fe_3O_4 ferromagnetic microspheres has demonstrated the ability of these materials to deliver heat in a controllable way via induction heating (to between 40–45 °C), thereby addressing one of the main requirements for MHT.[46] It is also notable that the rapid, flame spheroidization process has enabled the novel combination of phosphate-based glass and magnetite, with the resulting glass-ceramic products retaining ferromagnetic expression.

The P40-Fe_3O_4 microsphere products showed good levels of homogeneity, in terms of size and porosity levels. Comprehensive mineral analysis data showed that P40-Fe_3O_4 porous microspheres comprised a mixture of pure P40 and modified Ca-P40-Fe matrices embedded with Fe minerals (primarily Fe_3O_4 and $Ca_2Fe_2O_5$). The findings of MLA investigations were reinforced by EDS mapping, highlighting FeO-rich regions (≈10 µm) distributed within P40 microsphere matrices (125–212 µm). Further, an association of (unreacted) Fe_3O_4 and (reacted) $Ca_2Fe_2O_5$ with FeO-rich areas dispersed within the glass matrices was confirmed, with these regions considered responsible for ferromagnetic expression and the induction heating profiles of the P40-Fe_3O_4 porous microspheres.

The highly porous P40-Fe_3O_4 ferromagnetic microspheres were produced by feeding prepared powders into a high-temperature oxygen-acetylene flame (≈3100 °C) where they melted and coalesced, and acquired spherical form due to surface tension

ADVANCED MATERIALS INTERFACES
Open Access
www.advmatinterfaces.de

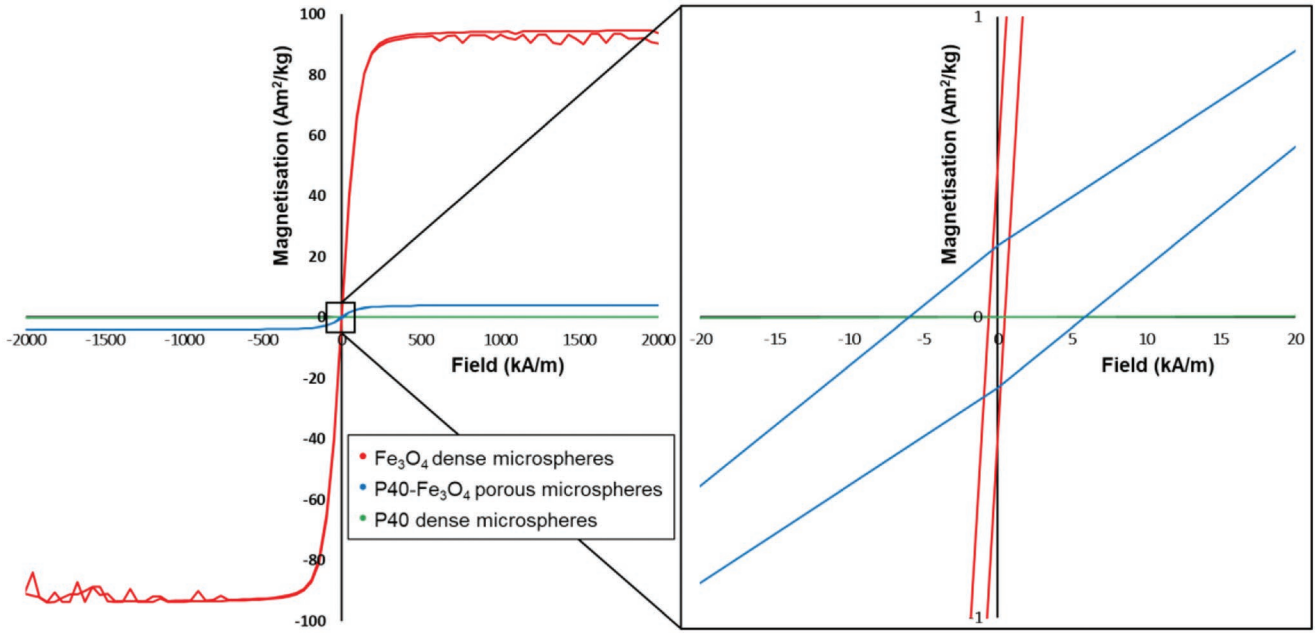

Figure 5. SQUID magnetometry measurements for flame-processed P40-Fe_3O_4 porous microspheres, compared to reference Fe_3O_4 and P40 dense microspheres, at 26.85 °C. Enlarged figure provides evidence for Fe_3O_4 and P40-Fe_3O_4 remanent magnetization.

and rapid cooling upon ejection from the flame (**Figure 8**). It is considered that the high levels of porosity arose from a combination of physical and chemical parameters, i.e., precursor melting point, viscosity and porogen concentration.[45,47] In the present study, the melting points for P40 glass (≈765 °C)[45] and magnetite (≈1600 °C) were sufficiently low for molten droplet formation within the flame, while levels of melt viscosity were appropriate for CO_2 entrapment and release. $CaCO_3$ porogen decomposition (*Reaction 1*) was considered responsible for CO_2 production and release prior to particle cooling and solidification, leading to development of the microsphere interconnected porosity observed.[44] Further, XRD data revealed the presence of Fe_2O_3, attributed to Fe_3O_4 oxidation (*Reaction 2*). It is noted that $Ca_2Fe_2O_5$ emerges as a consequence of reaction of CaO with Fe_2O_3 (*Reaction 3*).[44] Moreover, correlation of FeO-rich areas with high levels of CaO was consistent with the chemical affinity of Fe_3O_4 and $CaCO_3$ to develop $Ca_2Fe_2O_5$. Hence, it is suggested that FeO-rich regions here comprise a ferromagnetic $Ca_2Fe_2O_5$ perovskite type structure,[48] and within $Ca_2Fe_2O_5$ there is evidence (Table 1) also on the incorporation of other constituents upon solidification, i.e., P_2O_5, Na_2O, and MgO. In the case of flame-processed Fe_3O_4 and P40 control samples, in the absence of $CaCO_3$, topographical evidence confirmed the development of dense microspheres, thereby emphasizing the importance of CO_2 on porosity formation.

$$CaCO_3 \rightarrow CaO + CO_2 \quad (1)$$

$$4Fe_3O_4 + O_2 \rightarrow 6Fe_2O_3 \quad (2)$$

$$2CaO + Fe_2O_3 \rightarrow Ca_2Fe_2O_5 \quad (3)$$

It is considered that the mechanism of heat generation within P40-Fe_3O_4 porous microspheres was via hysteresis loss, as the associated magnetization curves revealed remanent (i.e., residual) magnetization. This mechanism is typical for multi-domain, ferro- and ferrimagnetic materials,[10,33] and distinct from single-domain particles (i.e., superparamagnetic nanoparticles) that produce heat via Néel and Brownian relaxation.[33] For MHT applications, mediated by an internal heat source near to or inside a tumor (for example), microscale ferromagnetic bioactive glasses become an attractive option because the agglomeration of magnetic species (embedded in a solid matrix) is no longer an issue.[49] Additionally, it is noted that the experimental frequency used (204 kHz) was within the clinical accepted range for MHT.[11,46,50–54] Further, it has been reported that magnetic particles used in MHT should heat rapidly in order to prevent patient discomfort.[53] Notably, the target temperature (via induction coil heating) in this case was achieved in only 40 s. With regards to the relatively low magnetic fields established here, it is recognized that MHT effects can be readily achieved through the application

Table 2. Magnetic measurements for flame-processed reaction products.

Sample	Saturation magnetization [$Am^2\ kg^{-1}$ (or emu g^{-1})	Remanent magnetization/ Mr [$Am^2\ kg^{-1}$ (or emu g^{-1})]	Coercive field/Hc	
			[kA m^{-1}]	[Oe]
Fe_3O_4	93.7	0.8	0.5	6.7
P40-Fe_3O_4	4.0	0.2	5.8	72.6
P40	0	0	0	0

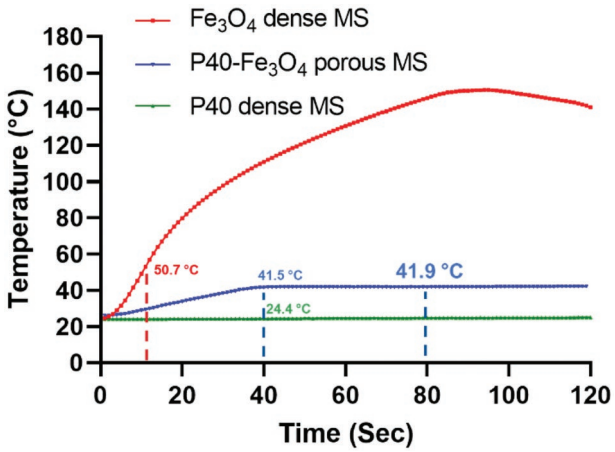

Figure 6. Induction heating curves for P40-Fe_3O_4 porous microspheres, compared with reference Fe_3O_4 and P40 dense microspheres (MS). (All curves display averages of triplicate measurements. Std. errors in Table S2, Supporting Information).

of weak magnetic fields (<7.95 kA m^{-1}).[53] Hence, it is evident that induction heating profiles for highly porous P40-Fe_3O_4 ferromagnetic microspheres are highly promising for MHT applications, whilst noting for validation this would need formal investigation in a clinical alternating magnetic field environment in the future.

Table 3. Experimental parameters for induction heating experiments.

Voltage [V]	Power [W]	Current [A]	Magnetic field [kA m^{-1} (Oe)]	Frequency [kHz]
250	350	1.4	0.17 (2.2)	204
100	120	1.2	0.15 (1.9)	204

The cytocompatibility studies indicated the general suitability of P40-Fe_3O_4 porous microspheres for healthcare applications. The MG-63 cells evaluated on days 2 and 7 showed P40-Fe_3O_4 porous microspheres exhibited sustained, higher levels of metabolic activity as compared to control Fe_3O_4 and P40 dense microsphere samples. Complementary ESEM investigations for day 7 samples revealed evidence for good conformation of MG-63 cells on P40-Fe_3O_4 microspheres, guided by surface texture, suggesting that these cells would colonize porous glass-ceramics preferentially.[55] Indeed, P40 porous microspheres have been shown previously to be cytocompatible and biocompatible via in vivo studies.[42,56] It is evident here that the P40 matrix increases considerably the cytocompatibility of P40-Fe_3O_4 microsphere products compared to the dense controls. The initial low metabolic activity of P40 dense microspheres, on day 2, was attributed to the presentation of a low surface area compared to the porous microspheres. Hence, the enhanced cytocompatibility associated with magnetite incorporated within

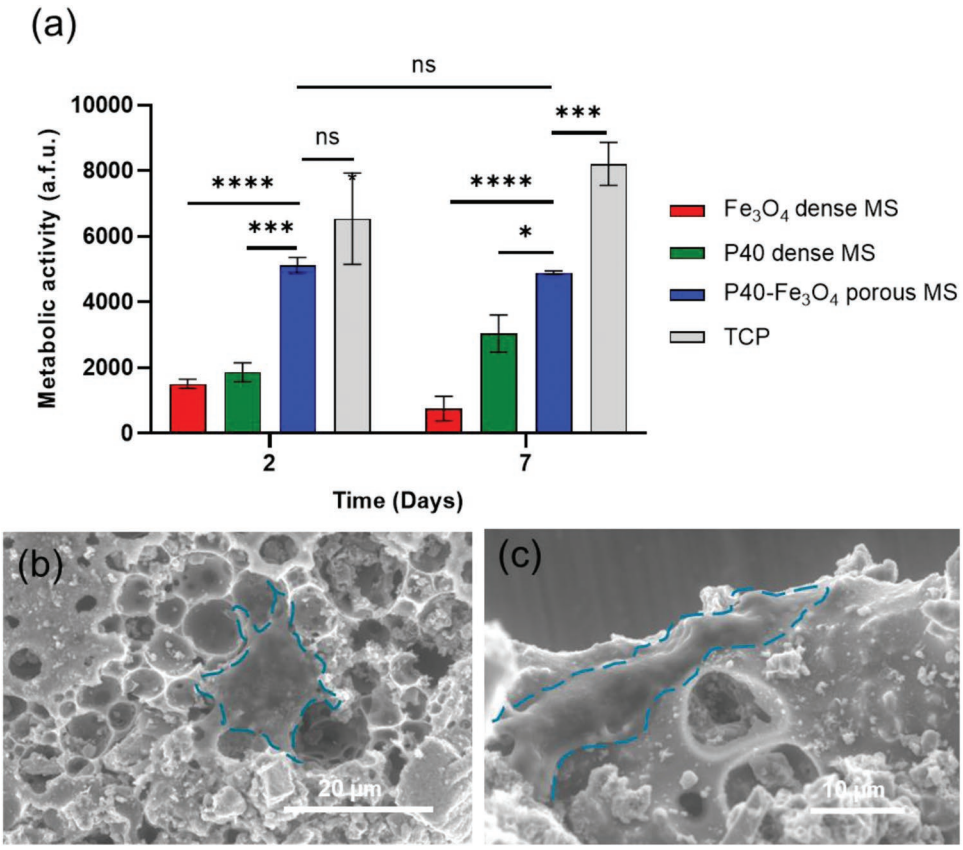

Figure 7. Evaluation of cell growth and ESEM imaging, in direct culture, of human osteoblast derived MG-63 adhered to P40-Fe_3O_4 microspheres. a) Cell metabolic activity on days 2 and 7 for P40-Fe_3O_4 porous microspheres, compared to Fe_3O_4 and P40 dense microspheres (ns = no significance; *$p < 0.05$; ***$p < 0.0007$; and ****$p < 0.0001$). b,c) High magnification ESEM images of cell seeded P40-Fe_3O_4 porous microspheres on day 7. Blue dashed lines illustrate cell peripheries. (Arbitrary fluorescence units (a.f.u.); Tissue culture plastic (TCP)).

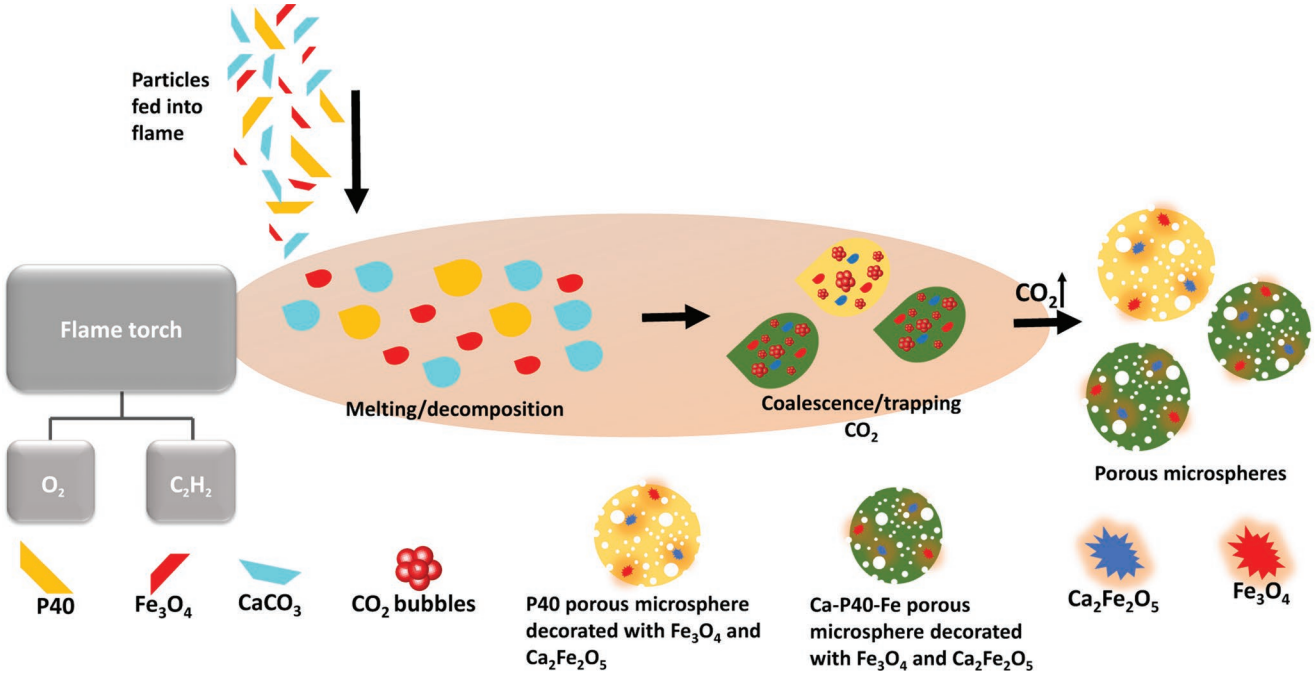

Figure 8. Schematic representation of the flame spheroidization process for magnetic glass-ceramic microsphere production.

larger, porous P40 microspheres suggests larger surface area provides a significant advantage for cell proliferation.

Depending on the target tissue, it is noted that porous microspheres may be delivered via oral, inhalation, implantation or intratumoral approaches. For example, injectable bone cements in conjunction with microspheres have been investigated for osteogenic applications[57] and drug-delivery.[58] Similarly, hydrogels embedded with bioactive glasses have been reportedly delivered via minimally invasive injection (cannulated needle or catheter).[59] For the case of osteosarcoma, locally delivered strategies combining therapeutic approaches have been reported, e.g., hydrogels embedded with porous microspheres for drug delivery via patch implantation;[60] thermosensitive hydrogels in combination with chemotherapeutics delivered by intratumoral injection;[61] or Fe_3O_4 and CaO_2 nanoparticles loaded into a 3D printed akermanite scaffolds for synergistic MHT with catalytic suppression therapy, delivered via implantation.[62]

In this context, there is high potential for the development of P40-Fe_3O_4 porous ferromagnetic microspheres, in combination with hydrogels or bone cements, for MHT applications. In particular, high porosity levels could provide an opportunity for the incorporation and delivery of various payloads (drugs, biologics, cells, etc.) to specific tissue and/or location. Additionally, the rapid, single-stage, flame spheroidization process could provide for other unique glass-ceramic combinations, with enhanced cytocompatibility combined with porosity.

5. Conclusions

Highly porous, cytocompatible, glass-ceramic ferromagnetic microspheres have been manufactured for the first time via a facile, rapid, single-stage flame spheroidization process, using ground powder mixtures of P40, Fe_3O_4, and $CaCO_3$. Complementary SEM, XRD, EDS, and MLA investigations confirmed a distribution of ≈10 µm sized Fe_3O_4 and $Ca_2Fe_2O_5$ phases embedded within 125–212 µm sized P40-based microsphere glass-matrices, with evolution of CO_2 from the porogen considered responsible to the development of interconnected porosity upon solidification. SQUID magnetometry provided evidence for remanent magnetization (0.2 $Am^2\ kg^{-1}$) of the P40-Fe_3O_4 porous microspheres, while the dispersion of embedded ferromagnetic Fe_3O_4 and $Ca_2Fe_2O_5$ phases was attributed to the effective application of inductive heat, to a constant level of 41.9 °C, making these products highly appropriate for MHT applications. Further, human osteoblast-derived cell-culture investigations confirmed cytocompatibility and hence general suitability of these P40-Fe_3O_4 porous microspheres for healthcare applications, with complementary ESEM evidence showing good conformation of MG-63 cells on the microsphere surfaces. It is suggested that the demonstration of highly porous, cytocompatible, glass-ceramic microspheres, incorporating ferromagnetic expression, opens up new opportunities for the development of synergistic biomaterials, e.g. for localized magnetic hyperthermia treatments, combined with the potential to deliver therapeutics incorporated within the pore structures.

Supporting Information

Supporting Information is available from the Wiley Online Library or from the author.

Acknowledgements

J.M.D. would like to thank the National Council of Science and Technology (CONACyT) and the Faculty of Engineering, University

of Nottingham, for funding this work. With thanks also to the Henry Royce Institute for funding the SQUID characterization work-package, performed at Royce Discovery Centre, University of Sheffield. The authors also would like to acknowledge the Nanoscale and Microscale Research Centre (nmRC), and Dr. Colin Scotchford from Faculty of Engineering, University of Nottingham, for use of their instruments and facilities.

Conflict of Interest

The authors declare no conflict of interest.

Data Availability Statement

The data that support the findings of this study are available from the corresponding author upon reasonable request.

Keywords

bioactive glasses, magnetic hyperthermia, magnetic particles, porous microspheres

Received: September 20, 2022
Revised: January 10, 2023
Published online:

[1] H. Sung, J. Ferlay, R. L. Siegel, M. Laversanne, I. Soerjomataram, A. Jemal, F. Bray, *Ca-Cancer J. Clin.* **2021**, *71*, 209.
[2] E. Sharifi, A. Bigham, S. Yousefiasl, M. Trovato, M. Ghomi, Y. Esmaeili, P. Samadi, A. Zarrabi, M. Ashrafizadeh, S. Sharifi, R. Sartorius, F. D. Moghaddam, A. Maleki, H. Song, T. Agarwal, T. K. Maiti, N. Nikfarjam, C. Burvill, V. Mattoli, M. G. Raucci, K. Zheng, A. R. Boccaccini, L. Ambrosio, P. Makvandi, *Adv. Sci.* **2022**, *9*, 2102678.
[3] L. Zhong, Y. Li, L. Xiong, W. Wang, M. Wu, T. Yuan, W. Yang, C. Tian, Z. Miao, T. Wang, S. Yang, *Signal Transduction Targeted Ther.* **2021**, *6*, 201.
[4] S. Senapati, A. K. Mahanta, S. Kumar, P. Maiti, *Signal Transduction Targeted Ther.* **2018**, *3*, 7.
[5] B. Lin, F. Gao, Y. Yang, D. Wu, Y. Zhang, G. Feng, T. Dai, X. Du, *Front. Oncol.* **2021**, *11*.
[6] E. J. Moding, M. B. Kastan, D. G. Kirsch, *Nat. Rev. Drug Discov.* **2013**, *12*, 526.
[7] A. Rajan, N. K. Sahu, *J. Nanopart. Res.* **2020**, *22*, 319.
[8] Y. lian, L. Wang, J. Cao, T. Liu, Z. Xu, B. Yang, T. Huang, X. Jiang, N. Wu, *Adv. Compos. Hybrid Mater.* **2021**, *4*, 925.
[9] I. Hilger, *Int. J. Hyperthermia* **2013**, *29*, 828.
[10] D. Chang, M. Lim, J. Goos, R. Qiao, Y. Y. Ng, F. M. Mansfeld, M. Jackson, T. P. Davis, M. Kavallaris, *Front. Pharmacol.* **2018**, *9*, 831.
[11] X. Liu, Y. Zhang, Y. Wang, W. Zhu, G. Li, X. Ma, Y. Zhang, S. Chen, S. Tiwari, K. Shi, S. Zhang, H. M. Fan, Y. X. Zhao, X.-J. Liang, *Theranostics* **2020**, *10*, 3793.
[12] V. Safronov, E. Sozontov, M. Polikarpov, *J. Appl. Crystallogr.* **2015**, *48*, 690.
[13] I. Sato, M. Umemura, K. Mitsudo, H. Fukumura, J.-H. Kim, Y. Hoshino, H. Nakashima, M. Kioi, R. Nakakaji, M. Sato, T. Fujita, U. Yokoyama, S. Okumura, H. Oshiro, H. Eguchi, I. Tohnai, Y. Ishikawa, *Sci. Rep.* **2016**, *6*, 24629.
[14] Y. Fang, Y. He, C. Wu, M. Zhang, Z. Gu, J. Zhang, E. Liu, Q. Xu, A. M. Asrorov, Y. Huang, *Theranostics* **2021**, *11*, 6860.
[15] P. T. Yin, S. Shah, N. J. Pasquale, O. B. Garbuzenko, T. Minko, K. B. Lee, *Biomaterials* **2016**, *81*, 46.
[16] K. McNamara, S. A. M. Tofail, *Adv. Phys.: X* **2017**, *2*, 54.
[17] M. Johannsen, B. Thiesen, P. Wust, A. Jordan, *Int. J. Hyperthermia* **2010**, *26*, 790.
[18] K. Mahmoudi, A. Bouras, D. Bozec, R. Ivkov, C. Hadjipanayis, *Int. J. Hyperthermia* **2018**, *34*, 1316.
[19] A. Matsumine, K. Takegami, K. Asanuma, T. Matsubara, T. Nakamura, A. Uchida, A. Sudo, *Int. J. Clin. Oncol.* **2011**, *16*, 101.
[20] E. Ruiz-Hernández, M. C. Serrano, D. Arcos, M. Vallet-Regí, *J. Biomed. Mater. Res., Part A* **2006**, *79*, 533.
[21] A. Farzin, S. Hassan, R. Emadi, S. A. Etesami, J. Ai, *Mater. Sci. Eng., C* **2019**, *98*, 930.
[22] R. A. Rytov, V. A. Bautin, N. A. Usov, *Sci. Rep.* **2022**, *12*, 3023.
[23] Y. Rabin, *Int. J. Hyperthermia* **2002**, *18*, 194.
[24] D. Serantes, D. Baldomir, *Nanomaterials* **2021**, *11*, 2786.
[25] U. M. Engelmann, E. M. Buhl, S. Draack, T. Viereck, F. Ludwig, T. Schmitz-Rode, I. Slabu, *IEEE Magn. Lett.* **2018**, *9*, 1.
[26] R. Mejías, P. H. Flores, M. Talelli, J. L. Tajada-Herráiz, M. E. F. Brollo, Y. Portilla, M. P. Morales, D. F. Barber, *ACS Appl. Mater. Interfaces* **2019**, *11*, 340.
[27] A. A. Luderer, N. F. Borrelli, J. N. Panzarino, G. R. Mansfield, D. M. Hess, J. L. Brown, E. H. Barnett, E. W. Hahn, *Radiat. Res.* **1983**, *94*, 190.
[28] M. Miola, Y. Pakzad, S. Banijamali, S. Kargozar, C. Vitale-Brovarone, A. Yazdanpanah, O. Bretcanu, A. Ramedani, E. Vernè, M. Mozafari, *Acta Biomater.* **2019**, *83*, 55.
[29] J. Crush, A. Hussain, K. T. M. Seah, W. S. Khan, *Front. Cell Dev. Biol.* **2021**, *9*, 643781.
[30] O. Sedighi, A. Alaghmandfard, M. Montazerian, F. Baino, *J. Am. Ceram. Soc.* **2022**, *105*, 1723.
[31] M. N. Rahaman, D. E. Day, B. S. Bal, Q. Fu, S. B. Jung, L. F. Bonewald, A. P. Tomsia, *Acta Biomater.* **2011**, *7*, 2355.
[32] M. T. Islam, R. M. Felfel, E. A. Abou Neel, D. M. Grant, I. Ahmed, K. M. Z. Hossain, *J. Tissue Eng.* **2017**, *8*, 204173141771917.
[33] M. V. Velasco, M. T. Souza, M. C. Crovace, A. J. A. d. Oliveira, E. D. Zanotto, *Biomed., Ther. Clin. Appl. Bioact. Glasses* **2019**, *5*, 148.
[34] Y. Cai, Y. Chen, X. Hong, Z. Liu, W. Yuan, *Int. J. Nanomed.* **2013**, *8*, 1111.
[35] D. G. Dastidar, S. Saha, M. Chowdhury, *Int. J. Pharm.* **2018**, *548*, 34.
[36] M. T. Islam, N. A. Nuzulia, L. Macri-Pellizzeri, F. Nigar, Y. W. Sari, I. Ahmed, *J. Biomater. Appl.* **2022**, *36*, 1427.
[37] B. Arifvianto, J. Zhou, *Materials* **2014**, *7*, 3588.
[38] H. Cai, W. Mu, W. Liu, X. Zhang, Y. Deng, *Inorg. Chem. Commun.* **2015**, *51*, 71.
[39] S. Hooshmand, J. Nordin, F. Akhtar, *Int. J. Ceram. Eng. Sci.* **2019**, *1*, 77.
[40] M. A. A. M. Nor, L. C. Hong, Z. A. Ahmad, H. Md Akil, *J. Mater. Process. Technol.* **2008**, *207*, 235.
[41] Y. J. Tan, X. Tan, W. Y. Yeong, S. B. Tor, *Sci. Rep.* **2016**, *6*, 39140.
[42] K. M. Z. Hossain, U. Patel, A. R. Kennedy, L. Macri-Pellizzeri, V. Sottile, D. M. Grant, B. E. Scammell, I. Ahmed, *Acta Biomater.* **2018**, *72*, 396.
[43] K. M. Z. Hossain, U. Patel, I. Ahmed, *Prog. Biomater.* **2015**, *4*, 1.
[44] J. Molinar Díaz, S. A. Samad, E. Steer, N. Neate, H. Constantin, M. T. Islam, P. D. Brown, I. Ahmed, *Mater. Adv.* **2020**, *1*, 3539.
[45] M. T. Islam, L. Macri-Pellizzeri, K. M. Z. Hossain, V. Sottile, I. Ahmed, *Mater. Sci. Eng., C* **2021**, *120*, 111668.
[46] Z. Shaterabadi, G. Nabiyouni, M. Soleymani, *Prog. Biophys. Mol. Biol.* **2018**, *133*, 9.
[47] D. Gupta, K. M. Z. Hossain, I. Ahmed, V. Sottile, D. M. Grant, *ACS Appl. Mater. Interfaces* **2018**, *10*, 25972.

[48] B. F. Amorim, M. A. Morales, F. Bohn, A. S. Carriço, S. N. de Medeiros, A. L. Dantas, *Phys. B* **2016**, *488*, 43.
[49] S. S. Danewalia, K. Singh, *Mater. Today Bio* **2021**, *10*, 100100.
[50] D. Kouzoudis, G. Samourgkanidis, A. Kolokithas-Ntoukas, G. Zoppellaro, K. Spiliotopoulos, *Front. Mater.* **2021**, *8*.
[51] R. Hergt, S. Dutz, *J. Magn. Magn. Mater.* **2007**, *311*, 187.
[52] A. S. Khan, M. F. Nasir, M. T. Khan, A. Murtaza, M. A. Hamayun, *Phys. B* **2021**, *600*, 412627.
[53] C. S. S. R. Kumar, F. Mohammad, *Adv. Drug Delivery Rev.* **2011**, *63*, 789.
[54] J.-H. Park, A. M. Derfus, E. Segal, K. S. Vecchio, S. N. Bhatia, M. J. Sailor, *J. Am. Chem. Soc.* **2006**, *128*, 7938.
[55] J. V. Wandiyanto, V. K. Truong, M. Al Kobaisi, S. Juodkazis, H. Thissen, O. Bazaka, K. Bazaka, R. J. Crawford, E. P. Ivanova, *Materials* **2019**, *12*, 1575.
[56] J. S. McLaren, L. Macri-Pellizzeri, K. M. Z. Hossain, U. Patel, D. M. Grant, B. E. Scammell, I. Ahmed, V. Sottile, *ACS Appl. Mater. Interfaces* **2019**, *11*, 15436.
[57] S. Tan, Y. Wang, Y. Du, Y. Xiao, S. Zhang, *Bioact. Mater.* **2021**, *6*, 3411.
[58] J. García-García, G. Azuara, O. Fraile-Martinez, C. García-Montero, M. A. Álvarez-Mon, S. Ruíz-Díez, M. Álvarez-Mon, J. Buján, N. García-Honduvilla, M. A. Ortega, B. De la Torre, *Polymers* **2022**, *14*.
[59] E. Zeimaran, S. Pourshahrestani, A. Fathi, N. A. b. A. Razak, N. A. Kadri, A. Sheikhi, F. Baino, *Acta Biomater.* **2021**, *136*, 1.
[60] X. Liu, K. A. Fundora, Z. Zhou, A. L. Miller2nd, L. Lu, *Tissue Eng., Part A* **2019**, *25*, 172.
[61] H. Shan, K. Li, D. Zhao, C. Chi, Q. Tan, X. Wang, J. Yu, M. Piao, *Front. Pharmacol.* **2020**, *11*, 573.
[62] S. Dong, Y. Chen, L. Yu, K. Lin, X. Wang, *Adv. Funct. Mater.* **2020**, *30*, 1907071.